JOURNAL OF PROPULSION AND POWER
Vol. 21, No. 6, November–December 2005

Unsteady Off-Design Velocity and Reynolds Stresses in an Axial Compressor

G.-J. Michon,* H. Miton,† and N. Ouayahya‡
Université Pierre-et-Marie-Curie, 75252 Paris, France

The aim of the present work is to provide unsteady experimental data about the flow in a one-stage axial compressor. Some particular flow features are described and discussed. The operating conditions considered here concern an off-design point that is close to the compressor rotating stall limit. Measurements were performed with a three-dimensional laser Doppler velocimeter. Twenty-eight axial sections were surveyed from the rotor inlet to the stator outlet. In each section, velocity and velocity fluctuation measurements concerned more than 250 points. Thus, more than 8000 locations of measurement were investigated in the rotating and in the fixed parts of the stage. The main flow patterns associated with the rotor unsteadiness are described through a few pictures of the measured velocity components and of the Reynolds-stress distributions. Obviously, the most outstanding flow phenomena occur in the upper part of the rotor channels and take place along the stator blades suction side. In the moving row, secondary complex flow structures are highlighted, and the structure of the separated flow along the stator blade is analyzed.

Nomenclature

C_x	=	axial blade chord at midspan
$(\boldsymbol{e}_b, \boldsymbol{e}_g, \boldsymbol{e}_y)$	=	unity vectors of the color frame of reference
f_{RTR}^{-1}	=	rotor blade passing period
H	=	channel height
h	=	height
k	=	phase of a collected sample
$\dot{m}$	=	mass-flow rate
R_{tip}	=	radius at rotor-blade tip
U	=	peripheral velocity of the rotor blades, $= \Omega \cdot R_{\mathrm{tip}}$
V	=	absolute velocity
$\boldsymbol{V}$	=	absolute velocity vector in the cylindrical compressor frame
$\boldsymbol{V}_{\mathrm{color}}$	=	velocity vector in the color frame of reference
W	=	relative velocity
$\boldsymbol{W}$	=	relative velocity vector in the cylindrical compressor frame
(x, R, θ)	=	cylindrical system of coordinates (x is the engine axis)
θ_{RTR}	=	azimuthal coordinate in the cylindrical relative frame of the rotor
λ	=	color wavelength
τ_{xx}	=	component of the Reynolds tensor in the axial direction
$\tau_{x\theta}$	=	component of the Reynolds tensor in the x, θ direction
$\tau_{\theta\theta}$	=	component of the Reynolds tensor in the tangential direction

Subscripts

b	=	relative to the blue ($\lambda = 488$ nm) color
g	=	relative to the green ($\lambda = 514$ nm) color
RTR	=	relative to the rotor
STR	=	relative to the stator
y	=	relative to the yellow-green ($\lambda = 532$ nm) color
Ω	=	rotor angular velocity

Superscripts

-	=	steady mean value
$\sim$	=	phase-averaged value
$'$	=	turbulent fluctuation

Received 7 May 2004; revision received 2 February 2005; accepted for publication 7 February 2005.

*Research Engineer, Laboratoire d'Energétique et de Mécanique des Fluides Interne, Unité Associée au Centre National de Recherche Scientifique.

†Researcher, Laboratoire d'Energétique et de Mécanique des Fluides Interne, Unité Associée au Centre National de Recherche Scientifique.

‡Research Assistant, Laboratoire d'Energétique et de Mécanique des Fluides Interne, Unité Associée au Centre National de Recherche Scientifique.

Introduction

THE evolution of the axial compressors used for aeronautical applications tends to decrease the number of stages as well as their axial length. Consequently, the spacing between the rotor and the stator is reduced. Strong pressure and velocity gradients appear as a result of the unsteady rotor-stator interaction. Many numerical predictions of the flow are nowadays available,[1] but there is still a need for detailed experiments to confirm the validity of the computational-fluid-dynamics (CFD) results and to obtain information about particular aspects of the flow physics. The first turbomachinery application of laser Doppler velocimetry was conducted by Wisler and Mossey[2] in a compressor rotor passage with a one-component system. Twenty years later, for the first time, Chesnakas and Dancey[3] instrumented an axial compressor with a three-dimensional laser system. Stauter[4] explored the tip region flowfield in an axial compressor with an original three-dimensional system emitting five laser beams of only two colors. Laser Doppler velocimetry was used to determine the three-dimensional velocity field with a three component laser system by Hathaway et al.[5] inside a centrifugal compressor and by Faure et al.[6] inside the present axial compressor. Nevertheless, flow investigation is not limited to the mean velocity, and information about the turbulent fluctuations is also a source of interest.

Indeed, the determination of the Reynolds-stress components is useful to a better understanding, and hence improved modeling, of the turbulence structure, the diffusion process, or the complex disturbances such as the secondary flows, for example. For this reason, various experimental investigations have been conducted over an extended period. Thus, the turbulence kinetic energy and the Reynolds-stress fields have been deduced from measurements by means of hot wires and pressure transducers by Ubaldi et al.[7] downstream of a backward-swept centrifugal impeller and also in detail by Pinarbasi and Johnson[8] within the diffuser of a centrifugal compressor using a triple hot-wire probe. In axial turbomachinery,

Ravindranath and Lakshminarayana,[9] Inoue and Kuroumaru,[10] and Sentker and Riess[11] investigated the turbulence structure with this kind of intrusive instrumentation. Some of these studies pointed out the anisotropic nature of the turbulence and evaluated the important role of the Reynolds stresses in the mixing process. Experimental studies with the same objective using nonintrusive instruments are less numerous in the literature.

A two-component laser velocimeter was used for turbulence measurements inside and downstream of a turbine rotor passage by Zaccaria and Lakshminarayana[12] showing the interaction of the stator wake with the flow near the rotor-blade pressure side and its influence on the decay of the turbulent wake properties. A three-dimensional laser-Doppler-velocimeter system was used on the same setup to explore the turbulent flow between the nozzle and the rotor by Ristic et al.[13] This study showed the cross correlations associated with the velocity gradient of the wake deficit and identified the counter-rotating secondary flows in the blade passage.

Regarding flow in axial compressors, many recent studies have been carried out, but they are generally limited to the nonrotating parts of the machine. Foley and Ivey[14] made pneumatics measurements between the rows of a compressor and laser transit velocimetry measurements inside the rotor-casing flow to measure the tip clearance flow in a multistage axial compressor. Suder et al.[15] and Suder and Celestina[16] paid attention to the tip clearance flow and to the influence of blade thickness and roughness in a transonic compressor flow. The three-dimensional mean velocity field has been measured by laser Doppler velocimetry in a high-speed compressor.[17] Particular attention was devoted to the hub corner stall influence on the performance of an axial compressor blade row by numerical simulation and oil flow visualization on the blade and hub surfaces.[18] Hub corner stall, responsible for high loss region, was also observed by Schulz and Gallus[19] at the exit of an isolated subsonic compressor stator at off-design operating points. An extensive range of operating points from design to stall was also studied by Popovski and Lakshminarayana,[20] and Schreeve et al.,[21] respectively, in a compressor rotor and a compressor cascade.

The availability of detailed unsteady measurements with turbulent stress determination performed using laser velocimetry within the stage of an axial compressor, including the moving row, is however still limited. In a previous work,[6] the unsteady velocity field within the entire stage of the CME_2 compressor was presented at the design operating point ($\dot{m} = 10.5\ \mathrm{kg \cdot s^{-1}}$, N = 6330 rpm). This study was performed using a two-component laser Doppler velocimeter. All of the components of the velocity were evaluated using a dual probe orientation at each point of measurement. The purpose of the present work is to extend the investigation to a reduced mass-flow rate operating point close to the occurence of rotating stall in the CME_2 compressor. Moreover, the new set of measurements presented was performed using a fully three-dimensional laser Doppler velocimeter.

Such experimental studies are essential to get an improved understanding of the behavior and phenomena of the flow in a machine through direct observation and a relevant analysis. In addition, quantitative data are provided to assess and calibrate the results of CFD codes. For this purpose, an experimental database including a grid of more than 8000 points of measurement within the entire compressor stage was built. It includes the three unsteady components of the velocity and the stress components deduced from the fluctuations of the velocity (ensemble phase averaged).

The aim of this paper is to analyze the major structure of the experimentally observed flowfield. In a first part, the experimental setup and the flow measurement process are described. Then, the properties of the fields of the unsteady velocity and stresses are presented in both rows.

Experimental Facility and Instrumentation

Test Rig

The single-stage axial compressor CME_2 setup is shown in Fig. 1. An inlet filtering system of the atmospheric air, a settling chamber followed by the compressor test rig, a flow adjuster, and an outlet duct discharging into the room compose this open-circuit facility. The rotor is powered by an electrically driven motor that delivers a maximum of 180 kW with a maximum rotating speed of 3000 rpm. The rotor speed is increased by a gear box allowing a maximum rotational speed of the shaft equal to 7000 rpm (ratio 2.345).

The mass-flow rate is regulated by the axial displacement of the hub wall downstream of the compressor rig outlet. This wall is driven by an electrical dc motor. Inlet and outlet temperatures are obtained from platinum resistance gauges introduced radially in the compressor. Total pressure probes are used to estimate the compressor pressure ratio. The entire test rig is surveyed and driven by an A/D I/O board through a PC.

Compressor CME_2

The CME_2 compressor stage (Fig. 1) is fitted with a 30-blade rotor and a 40-blade stator. The axial length of the test section is 180 mm. The radius of the casing is 275 mm. The hub radius increases from 207 mm at the rotor inlet to 214 mm at the rotor outlet and then remains constant inside the stator row. The rotor-blade tip clearance equals 0.5 mm. A summary of the blade geometries is given in Tables 1 and 2. At the design operating point and with standard inlet conditions (a temperature of 15°C and a total pressure of 101,325 Pa), the rotational speed of the rotor is 6330 rpm (±14 rpm), and the mass-flow rate is 10.5 $\mathrm{kg \cdot s^{-1}}$ (±0.1 $\mathrm{kg \cdot s^{-1}}$), providing a total-to-total pressure ratio equal to 1.162.

Table 1 Rotor-blade geometry summary

Span	Chord, mm	Thickness, mm	Stagger angle, deg	Camber angle, deg
Hub	84	7.9	33.5	41.5
Mid	84	5.6	46	23
Tip	84	2.8	54	20

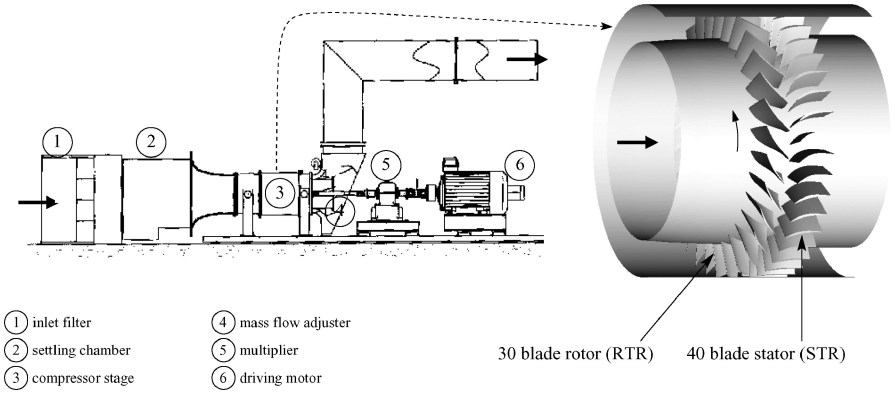

Fig. 1 Test rig and the compressor CME_2.

Table 2 Stator-blade geometry summary

Span	Chord, mm	Thickness, mm	Stagger angle, deg	Camber angle, deg
Hub	77	6.2	17.5	46.5
Mid	77	6.2	15	41.5
Tip	77	6.2	12.5	36

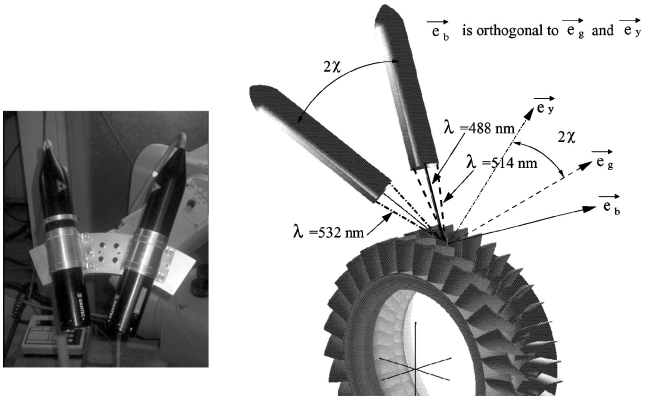

Fig. 2 View of the laser probes fixed on the robot arm and the three-dimensional laser probe system.

Laser-Doppler-Anemometer System

The laser Doppler anemometer (LDA) is a Dantec three-color measuring system, consisting of a two-dimensional probe and a one-dimensional probe (Fig. 2). Two different light sources are used. A 5-W argon-ion laser (Coherent Innova 305), tuned to 488 nm (blue) and 514.5 nm (green) wavelengths provides two colors for the two-dimensional laser head. To improve the intensity of the backscattered signal, another light source has been preferred to the 476.5-nm violet argon-ion spectral line for the third component. This source is a 2-W solid-state neodymium yttrium vanadate laser emitting a 532 nm (yellow-green) wavelength from the one-dimensional laser head. Each color beam is split in two. One of the split beams passes through a 40-Mhz Bragg cell, where it is frequency shifted to reduce the fringe bias and to allow the determination of the velocity direction. The half-angle between these two beams of the same wavelength is 6.772 deg, and the measuring volume is 0.8 mm in length and 0.1 mm in diameter.

The two probes are mounted on an optical support. The angle between their axes, denoted by 2χ, is 30 deg (Fig. 2). Note that the color frame of reference $(\boldsymbol{e}_b, \boldsymbol{e}_g, \boldsymbol{e}_y)$ attached to the fringes of the different wavelength beams is not orthogonal. The component of the velocity along the direction defined by the axis of the support is then

$$v_{\mathrm{ax}} = (v_g - v_y)\sin(\chi)$$

An increase of the angle χ would improve the accuracy of the determination of this velocity component. However, the problems caused by the blade mask will then be strongly increased. A value of χ equal to 15 deg is a satisfactory compromise in turbomachinery applications allowing especially the accurate evaluation of the unsteady periodic radial velocity component. However, the evaluation of the Reynolds tensor components τ_{xR}, $\tau_{R\theta}$, τ_{RR} is difficult. Excessively high values are often obtained because of an overestimation of the velocity fluctuations in the radial direction.

Spatial Positioning of the Measurement Volume

The support of the two laser probes is mounted in a six-degree-of-freedom robot. Its motion is controlled by the data-acquisition program, (Fig. 3). The issue is not only to move the probe volume from one point to another in the measurement mesh, but it is also possible to choose a relevant angle for the positioning of the measurement volume to reduce the mask of the blades. Thus, the laser heads can be yawed and pitched to avoid the crossing of a laser beam

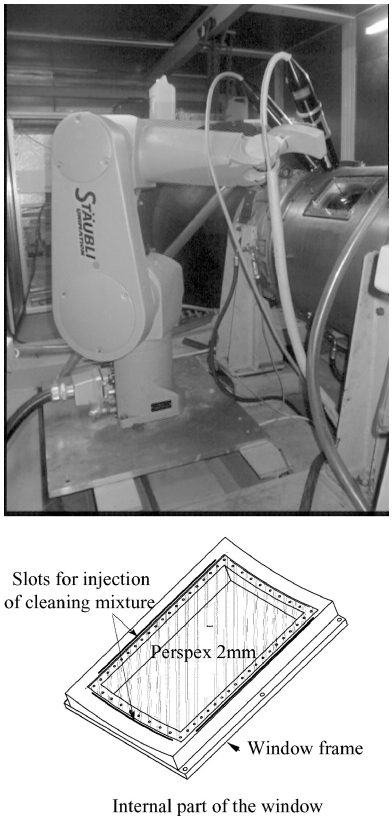

Fig. 3 View of the robot allowing an accurate positioning of the laser probes and the window of measurement.

with a blade surface. In addition, the digital operating mode of the robot enables very accurate positioning, because the repeatability of the displacement is approximately 20 μm. However, the real accuracy of the positioning depends on more parameters. First, it is necessary to teach the robot to link its frame of reference to that of the compressor. To accomplish this, three shallow tiny holes were drilled in the frame of the window glass. The procedure then consisted of moving the robot in manual mode to locate successively the measurement volume in each hole. The positions of the joints of the robot were then recorded by the computer. From the measurement of the three hole positions, it is easy to adjust the robot frame of reference in relation to that of the compressor. This procedure is quite accurate because when the light just enters the hole it is strongly diffracted. In this way, the accuracy of the positioning was estimated to be less than 0.1 mm. Another source of uncertainty of the positioning is associated with the vibration level of the compressor. Although this level is quite low, the robot basement was mounted on the machine frame to reduce, as far as possible, this effect.

Temporal Positioning of the Measurement Volume

The position of the measurement volume relative to the rotor blade is obtained by using a device mounted on the high-speed shaft of the compressor. Built around an infrared detector, it gives a level square-shaped signal at each revolution of the shaft. The detector has a cutoff frequency up to 0.1 Mhz. When correctly adjusted, this encoder is very accurate as shown by the recording of the signal continuously displayed on an oscilloscope. The effective resolution is much better than 1/24 of the rotor-blade pitch, which is the spacing used to display the instantaneous measurements.

Flow Seeding

The flow seeding is provided by a Safex 2001 smoke generator. This seeding material is obtained by heating a fluid containing glycerol, which was atomized into spherical droplets. According to the manufacturer, the average particle diameter is 1.068 μm with a

density of 1000 $kg \cdot m^{-3}$. The particles are injected in the flow in the settling chamber.

Window Glass

The flow parameters in the compressor are measured through a curved rectangular window which is 2 mm thick (Fig. 3). Made of Perspex, it conforms to the cylindrical shape of the compressor casing. Such a shape was considered necessary to avoid disturbances of the flow by minimizing the discontinuities in the casing wall especially in the rotor. The window is 200 mm long and 136 mm wide. Such an extension is allowed by the relatively low pressure ratio of the compressor. A region that covers azimuthally more than the equivalent of two contiguous stator channels can therefore be reached by the laser beams from casing to hub. Important experimental problems are, however, associated with this window.

1) First, it deviates the laser beams. The deviation of the beams affects the location of the measurement volume and the focus of the beams. The calculation of this effect was conducted by Pradère[22] and Vassilieff.[23] Because of the number of beams (six) to take into account, the results obtained are quite complex. Concerning the location of the measurement volume, it is shown that the best results are obtained when the plane of the two laser probes is parallel to the axis of the compressor. For such a configuration, the difference between the actual position of the point of measurement and the intended position has been computed for various angles of incidence between the beam direction and the normal direction of the window (the radial direction of the compressor frame). Of course, the difference between the positions depends on the direction considered. If the incidence is 15 deg., this difference is quite negligible (less than 20 μm) along the axial and tangential directions. For such an orientation of the laser probes, the results are not strongly dependent on the radius of curvature of the window. A simple correction is applied to the radial position of the point of measurement. Concerning the focus of the beams, it has been shown that the gap between the estimated center of the measurement volume and the individual beams is low (less than 60 μm). However, this does affect the data rate when the coincidence process is applied.

2) Long periods of measurement are necessary because many locations of measurement are investigated. During these periods, deposits of the seeding fluid affect the transparency of the window with respect to the backscattered light and drastically decrease the data-acquisition rate and can interrupt data acquisition. A cleaning system that periodically removes the deposits without stopping the compressor or removing the window was developed. It consists of injecting a water and soap mixture at two locations of the window frame. Used during a short time (3 s.) before each measurement operation, this system is quite efficient. The path of the liquid cleaning mixture on the glass is determined by the wall shear-stress field of the flow, and it is thus very difficult to clean a specified region of the internal glass surface.

Process of Data Collection

Contrary to the other instruments that run continuously, each component of the laser Doppler velocimeter performs an operation of measurement only each time a seeding particle crosses the volume of measurement. The three volumes of measurement have a common intersection, but they do not coincide one with another. Instants of measurement can then be different from one component to another. Each collection of data at a geometrical location is made up of an individual set of the couple time velocity associated with each color component of the velocimeter probes. Moreover, these velocity components, normal to the system of fringes in the measurement volume, are not orthogonal to one other. Let us define $\boldsymbol{V}_{\text{color}}(v_b, v_g, v_y)$ the vector of these components. The components of the absolute velocity vector $\boldsymbol{V}(v_x, v_R, v_\theta)$ expressed in the cylindrical frame of the compressor are obtained through a linear set of equations:

$$\boldsymbol{V}(M,t) = A(M,P) \cdot \boldsymbol{V}_{\text{color}}(M,t)$$

The matrix $A(M, P)$ connects the color frame of reference to the compressor frame of reference. It depends on the location M of the point and on the orientation P of the laser probes. It is calculated by the program controlling the attitude of the robot. Note that various parts of the velocity, unsteady, periodic, and fluctuating, are deduced from the preceding relation.

Definition of a Timescale

The complete duration of measurement is discretized using a set of times defined as

$$\mathrm{T}(l,k) = [l - 1 + (k-1)/N_k]\mathcal{T}$$

where l is the number of revolutions of the rotor, $\mathcal{T}$ is the period of rotation of the shaft, and N_k is a number defining the accuracy of the sequence. In the present work N_k has been chosen equal to 720. A complete revolution of the rotor is divided into 720 intervals. Let t be any time during a session of measurement. The values of l and k can be associated with t as

$$t = \mathrm{T}(l,k) \quad \text{if} \quad t \in [\mathrm{T}(l,k), \mathrm{T}(l,k+1)]$$

In practice, values of l and k are readily obtained using the recording of pulses provided by the shaft encoder. If t_i and t_{i+1} are the times of two successive pulses surrounding t,

$$k = int[N_k \cdot (t - t_i)/\mathcal{T}]$$

$$l = 1 + int[(t/\mathcal{T}) - (k-1)/N_k]$$

Ensemble Phase-Averaged Velocity

Let $V_{\text{color}}(M,t)$ be a velocity component measured at a time t in a location $M(x, R, \theta)$. The ensemble phase average of V_{color} will be defined as

$$\tilde{V}_{\text{color}}(M,k) = \sum_{l=1}^{N} \alpha(l,k) \cdot V_{\text{color}}[M, t(l,k)] \Big/ \sum_{l=1}^{N} \alpha(l,k)$$

where N is the total number of revolutions of the shaft during the session of measurement, $\alpha(l,k)$ is a gate taking into account the random characteristic of the data collection process. Then $\alpha(l,k) = 1$ if a particle is observed in the time interval $[\mathrm{T}(l,k), \mathrm{T}(l,k+1)]$, and $\alpha(l,k) = 0$ otherwise. Then,

$$\sum_{l=1}^{N} \alpha(l,k)$$

is the total number of samples collected in the phase k. Note that the number N of revolutions of the shaft has been chosen to collect a minimum of 30,000 samples for each session of measurement. The ensemble phase-averaging operator just defined is very close to the operator proposed by Adamczyk.[24]

Velocity Fluctuations

Fluctuations of velocity are obtained for each phase k through

$$V'_{\text{color}}(M,l,k) = \{V_{\text{color}}[M, t(l,k)] - \tilde{V}_{\text{color}}(M,k)\} \cdot \alpha(l,k)$$

and the cross correlations are obtained through

$$\overline{V'_{\text{color}_1} V'_{\text{color}_2}}(M,k) = \sum_{l=1}^{N} V'_{\text{color}_1}(M,l,k) \cdot V'_{\text{color}_2}(M,l,k) \Big/ \sum_{l=1}^{N} \alpha(l,k)$$

From the point of view of Adamczyk, these fluctuations are the nondeterministic fluctuations of the velocity. They include the turbulent fluctuations and all of the other fluctuations the characteristic periods of which are over the period of rotation of the shaft and also below $\mathcal{T}/N_k$ (the timescale of measurement).

However, deterministic velocity fluctuations could still be obtained as

$$V''_{\text{color}}(M,k) = \tilde{V}_{\text{color}}(M,k) - \hat{V}_{\text{color}}(M,k)$$

where

$$\hat{V}_{\text{color}}(M,k) = \sum_{k=1}^{N_k} \beta_k \cdot \tilde{V}_{\text{color}}(M,k) \Big/ \sum_{k=1}^{N_k} \beta_k$$

with β_k taking into account the metal blockage corresponding to the rotor blades ($\beta_k = 1$ if, at an instant t, the position defines a point located in the channel or on the blade surface; otherwise, $\beta_k = 0$).

In practice, the fluctuations of the velocity are not of great interest in themselves. Indeed, their influence is currently represented through the Reynolds tensor

$$\mathfrak{T}(M,k) = \begin{bmatrix} \tilde{\tau}_{xx} & \tilde{\tau}_{x\theta} & \tilde{\tau}_{xR} \\ \tilde{\tau}_{\theta x} & \tilde{\tau}_{\theta\theta} & \tilde{\tau}_{\theta R} \\ \tilde{\tau}_{Rx} & \tilde{\tau}_{R\theta} & \tilde{\tau}_{\text{RR}} \end{bmatrix} = \begin{bmatrix} \overline{v'_x v'_x} & \overline{v'_x v'_\theta} & \overline{v'_x v'_R} \\ \overline{v'_\theta v'_x} & \overline{v'_\theta v'_\theta} & \overline{v'_\theta v'_R} \\ \overline{v'_R v'_x} & \overline{v'_R v'_\theta} & \overline{v'_R v'_R} \end{bmatrix}$$

made of cross correlations between the velocity fluctuations.[25] Components of the Reynolds tensor are linearly dependent [through the coefficients of the matrix $A(M, P)$] on the component of the tensor

$$\mathfrak{T}_{\text{color}}(M,k) = \begin{bmatrix} \overline{v'_y v'_y} & \overline{v'_y v'_b} & \overline{v'_y v'_g} \\ \overline{v'_b v'_y} & \overline{v'_b v'_b} & \overline{v'_b v'_g} \\ \overline{v'_g v'_y} & \overline{v'_g v'_b} & \overline{v'_g v'_g} \end{bmatrix}$$

made of cross correlations between couples of color velocity fluctuation components defined above. To evaluate such cross-correlations, samples collected at the same time for two colors (bi-coincident samples) are used. Such samples are acquired much more frequently than tri-coincident samples collected at the same time for the three color components. The results presented here are based on the ensemble phase-averaged velocity components and on the velocity fluctuations.

Results and Discussion

Operating Point Definition

The present experimental investigations were carried out with working conditions corresponding to the design speed of rotation (6330 rpm) and a mass-flow rate of 9 $\text{kg} \cdot \text{s}^{-1}$ under standard conditions. This point of operation is close to the limit of stability of the compressor (8.57 $\text{kg} \cdot \text{s}^{-1}$). The location of this point is shown on the characteristic total-to-total pressure curve of the compressor (Fig. 4). The rotor-blade passing frequency f_{RTR} is equal to 3165 Hz.

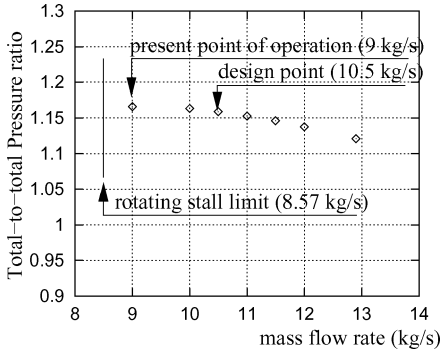

Fig. 4 Total-to-total pressure ratio characteristic of the compressor CME_2.

Locations of Measurement

Measurements were performed at 28 axial sections distributed over the entire compressor stage from upstream of the rotor inlet to the stator outlet (Fig. 5). In each axial section, a grid of measurement was defined. In the stator, the grids are limited by the casing, the hub, and also by the suction and pressure sides of adjacent blades. In the rotor and out of the bladed regions, the azimuthal extension of the grids is equal to 9 deg. It is quite lower in the stator because of the thickness of the blades. Sixteen nodes are regularly distributed in the azimuthal direction, and their number varies between 16 and 24 from the hub to the casing (Fig. 5). The number of nodes for each axial grid varies between 256 and 384. Thus, 8541 spatial locations of measurement were investigated in the compressor.

Generation of the Flow Pictures

Measurements were collected at discrete planes normal to the compressor axis. Under such circumstances, it is difficult to clearly observe phenomena that evolve outside the planes. For this reason, the measured velocities were projected onto a spatial grid characterized by an uniform density of nodes ($32 \times 32 \times 32$ for each of the rotating and stationary parts of the stage). To do this, each set of velocity obtained for given axial and radial locations has been represented through a set of its Fourier components calculated along the tangential direction. These Fourier components are then interpolated inside the refined grid. An inverse transformation of the interpolated Fourier components is used to reach the velocity vector or the Reynolds-stress components at each point of the refined mesh.

Overview of the Phase-Averaged Velocity Fields

The blade-to-blade periodic phase-averaged relative velocity fields are shown (Fig. 6) at three different spanwise locations ($h/H = 0.32$, 0.52, and 0.90). These fields are represented separately in the rotor and in the stator over four contiguous channels of the second row, assuming a chorochronic periodicity of the flow.[26]

Velocity Fields in the Rotor

Downstream of the rotor, the relative flow is mainly characterized by a strong interaction between the blade wakes and the potential effects of the stator blades (6A in Fig. 6), which induces a local velocity defect. Especially close to the casing ($h/H = 0.90$), these potential effects extend far upstream, appearing as local steady spots (6B in Fig. 6). These pictures give the main features of the flow in the rotor-blade channels. The mean gradient of the velocity is approximately parallel to the blade walls at all span locations. Except in the upstream region of the channels, the velocity difference between the pressure and the suction sides of the blades is approximately 10 $\text{m} \cdot \text{s}^{-1}$. So, the blade loading in the moving row is low. The boundary layers around the blades are not discernible. Because of the operating mode of the laser Doppler velocimeter, a synchronization between the rotating blades and the data acquisition is not

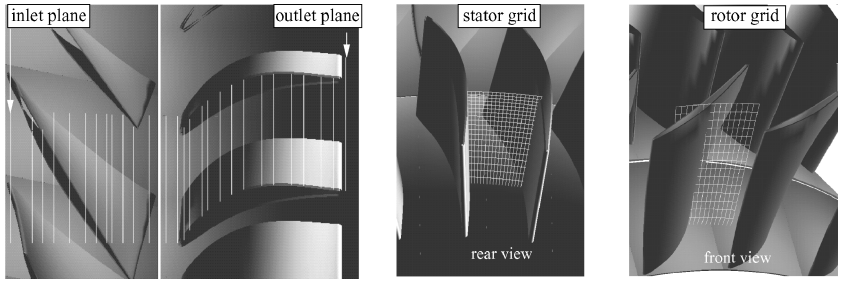

Fig. 5 Axial position of the sections and grids of measurement.

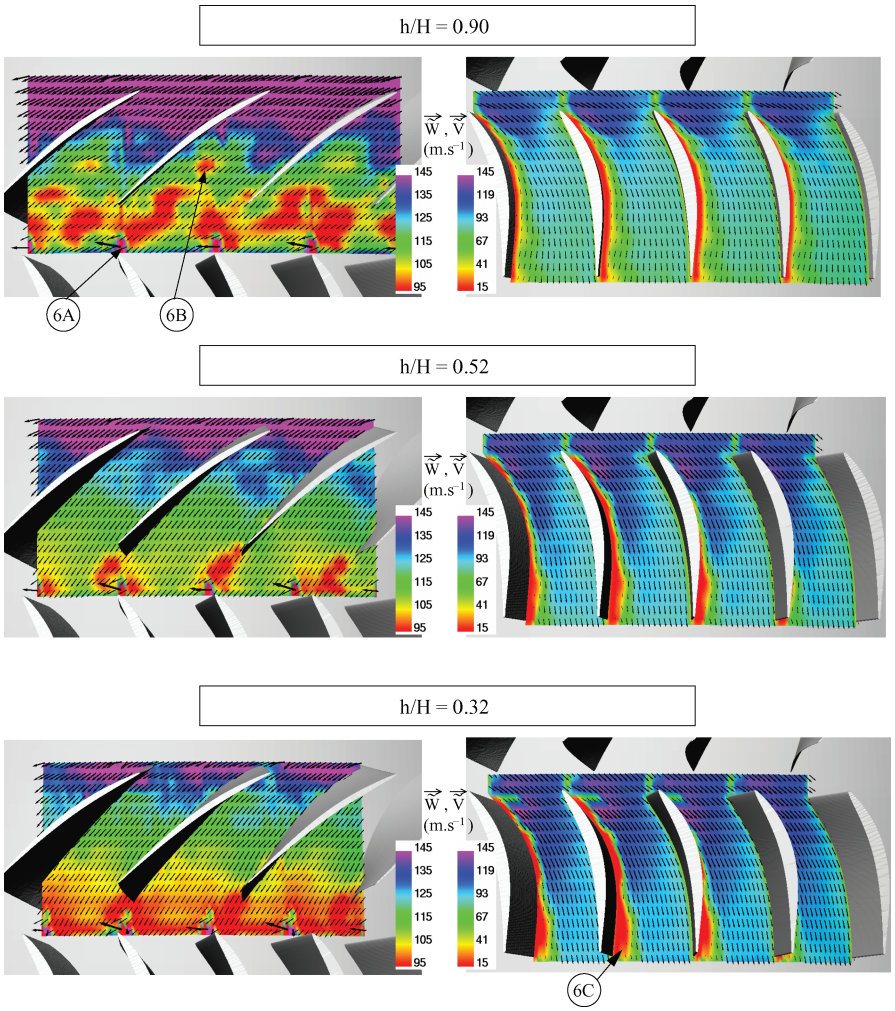

Fig. 6 Phase-averaged relative $\tilde{W}$ and absolute $\tilde{V}$ velocities at three spanwise locations within the CME_2 rotor row (left) and stator row (right); $\dot{m} = 9.0\ \mathrm{kg \cdot s^{-1}}$, $t/f_{\mathrm{RTR}}^{-1} = 0.375$.

possible; the measurements are not performed at times corresponding to discrete positions of the moving blades. So, if the thickness of the boundary layers is smaller than $(2\pi R_{\mathrm{tip}}/720) \simeq 2.4$ mm, they cannot be clearly detected. By considering the measured velocity field and the low value of the velocity gradient along the blade walls, the boundary-layer thickness is probably smaller than this value. The velocity defects caused by the wakes of the rotor blades are measured well. However, these relative velocity defects do not exceed $15\ \mathrm{m \cdot s^{-1}}$. For this reason, these wakes are difficult to observe on the vector field (Fig. 6), where the plotted vectors correspond to velocity magnitudes much longer than $15\ \mathrm{m \cdot s^{-1}}$.

To improve the analysis of the flow behavior within the CME_2 compressor stage, the pitchwise distributions of the phase-averaged relative and absolute velocities $\tilde{W}$ and $\tilde{V}$ are drawn at four different radii ($h/H = 0.32, 0.52, 0.70$, and 0.90) for two instants ($t/f_{\mathrm{RTR}}^{-1} = 0$ and $t/f_{\mathrm{RTR}}^{-1} = 0.5$) of the rotor-blade passing period (Fig. 7). Near the rotor inlet (PLANE_51: $x/\mathcal{C}_{x_{\mathrm{RTR}}} = 0.202$), the mean value of the relative velocity of the flow increases with the radius. From hub to tip, the acceleration of the fluid on the blade suction side increases, and, consequently, the blade-to-blade velocity gradient also grows in the spanwise direction. The difference between the minimum and the maximum values of $\tilde{W}$ is approximately $18\ \mathrm{m \cdot s^{-1}}$ at $h/H = 0.32$ and exceeds $48\ \mathrm{m \cdot s^{-1}}$ at $h/H = 0.90$. Note that, at each radius, the lowest value is not located on the pressure side but in the blade passage close to the pressure side. At PLANE_66 ($x/\mathcal{C}_{x_{\mathrm{RTR}}} = 0.853$), near the outlet of the moving row, the decrease of the relative velocity through the rotor is almost completed. A small gradient still exists in the pitchwise direction; the relative velocity is a little higher near the suction side. Contrary to what has been highlighted at PLANE_51, the velocity gradient vanishes at larger radii, but pitchwise fluctuations of $\tilde{W}$ express a certain disturbance of the flow at $h/H = 0.90$. It is interesting to observe that the local velocity deficit on the suction side increases because of the development of the blade wake. The mean value of $\tilde{W}$ increases slightly in the spanwise direction up to $h/H = 0.70$. It then drops at $h/H = 0.90$ mainly because of the flow disturbances; but the potential effects of the stator blades and the viscid effects are also important near the casing. These observations remain true whatever the time is because the flow shows little unsteadiness within the moving row. The only noticeable differences according to the time are located at the highest span ($h/H = 0.90$), where the intensity of the perturbations changes slightly with the rotor-blade position relative to the stator blades, modifying gently the velocity profile.

A finer observation of the phenomena occuring in the tip region is possible on Fig. 8, which shows the local periodic fluctuations of the velocity. They are obtained by subtracting the local time-mean velocity value from the phase-averaged one. The isocontours of this quantity are displayed (Fig. 8) on a surface at constant radius ($h/H = 0.935$) very close to the casing and on another surface at a fixed axial position ($x/\mathcal{C}_{x_{\mathrm{RTR}}} = 1.069$) just downstream of the moving row when $t/f_{\mathrm{RTR}}^{-1} = 0.25$ and 0.75. The wakes of the rotor blades (8A in Fig. 8) are characterized by a defect of the velocity fluctuation. The angle of the three-dimensional wakes relative to the radial direction increases as the wakes develop from the rotor trailing edge towards the stator inlet (see also Fig. 13). It denotes an azimuthal distortion of the wakes when they are convected in the

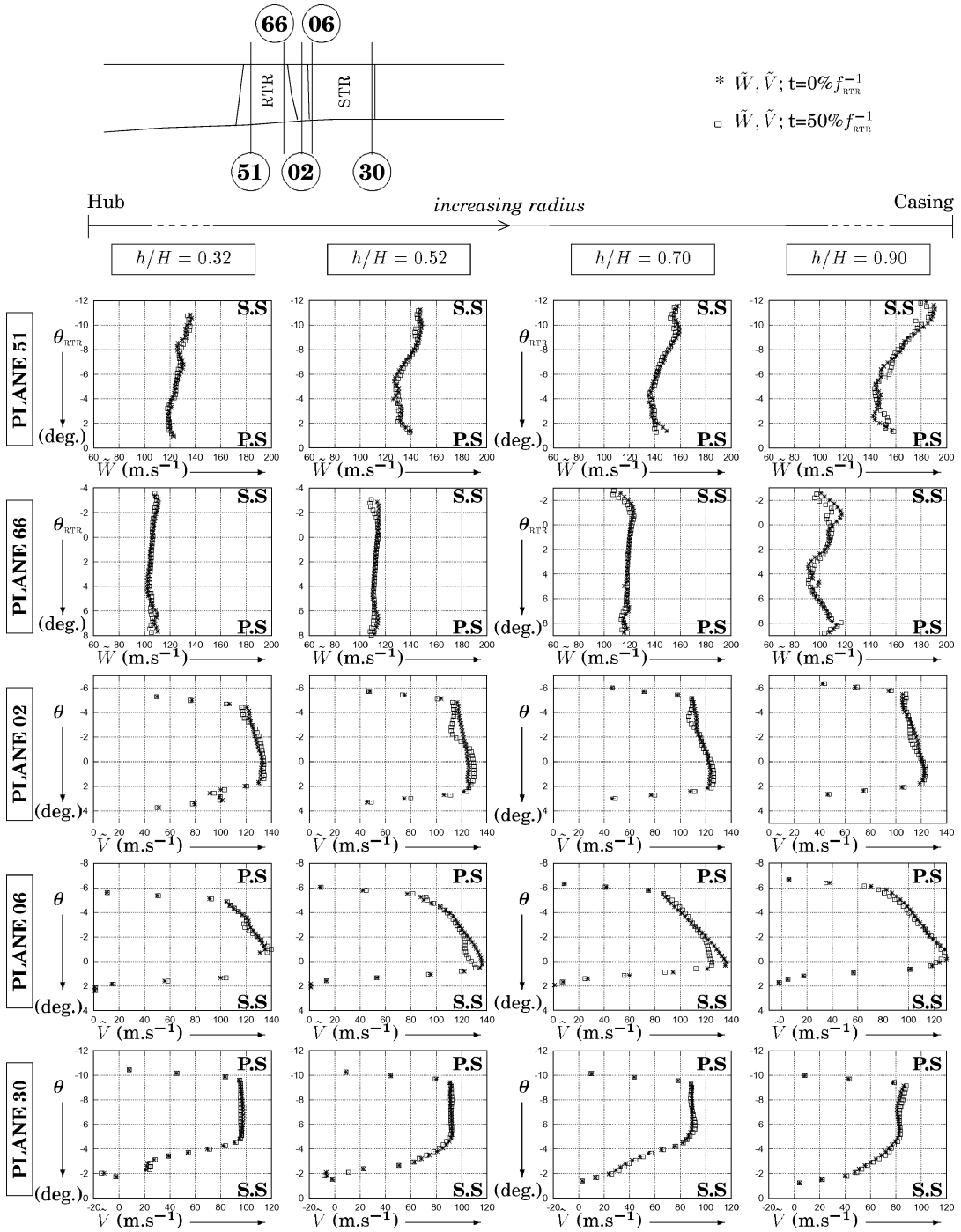

Fig. 7 Phase-averaged relative $\tilde{W}$ and absolute $\tilde{V}$ velocities; $\dot{m} = 9.0$ kg · s^{-1} (from left to right : 1st column, $h/H = 0.32$; 2nd column, $h/H = 0.52$; 3rd column, $h/H = 0.70$; 4th column, $h/H = 0.90$).

region between the rows. Near the casing, two regions where the velocity fluctuations are of an opposite sign are clearly observed at each phase of the rotor-blade passing period. Obviously, the flow is always accelerated on the blade suction side (8B in Fig. 8), and the velocity remains lower on the blade pressure side (8C in Fig. 8), but the difference between the mean values of the velocity in these two regions is only 10 m · s^{-1}. These regions are clearly defined. The region where the value of the velocity fluctuation is the lowest ($\tilde{W} - \bar{W} \leq -5.2$ m · s^{-1}) is slightly wider. The interface between the two regions is wavy in the streamwise direction because of the interaction of the flow with the potential effects of the stator blades that influence the flow far upstream of the fixed row. Downstream of the rotor, the mixing process is discernible. A part of the accelerated flow is deviated from the suction side towards the pressure side and rolls up round the region where the temporal fluctuation of the velocity is lower (8D in Fig. 8). Thus, a spot of overaccelerated flow is observed in the casing-trailing-edge corner on both blade sides. However, the blade loading is low, and the intensity of the secondary phenomena is limited. For this reason, the magnitude of the velocity is not the most convenient quantity to describe the three-dimensional flow features.

For this purpose, the mean value of the phase-averaged velocity relative to R, θ, and t was calculated at each axial section and subtracted from the local value of the phase-averaged velocity. The resulting field characterizes the spatiotemporal fluctuations of the velocity at each axial plane. This quantity is more suitable for analyzing the secondary flow phenomena in the rotating blade channels. The vector field of the spatiotemporal fluctuation of the azimuthal

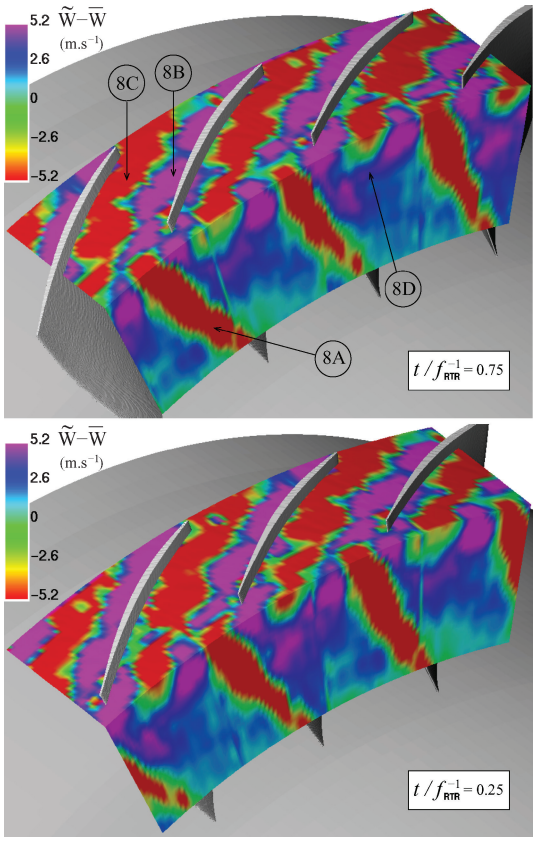

Fig. 8 Fluctuation of the relative phase-averaged velocity within the rotor row; $x/\mathcal{C}_{x_{RTR}} = 1.069$ and $h/H = 0.935$, $\dot{m} = 9.0$ kg · s^{-1}, $t/f_{RTR}^{-1} = 0.25$, and $t/f_{RTR}^{-1} = 0.75$.

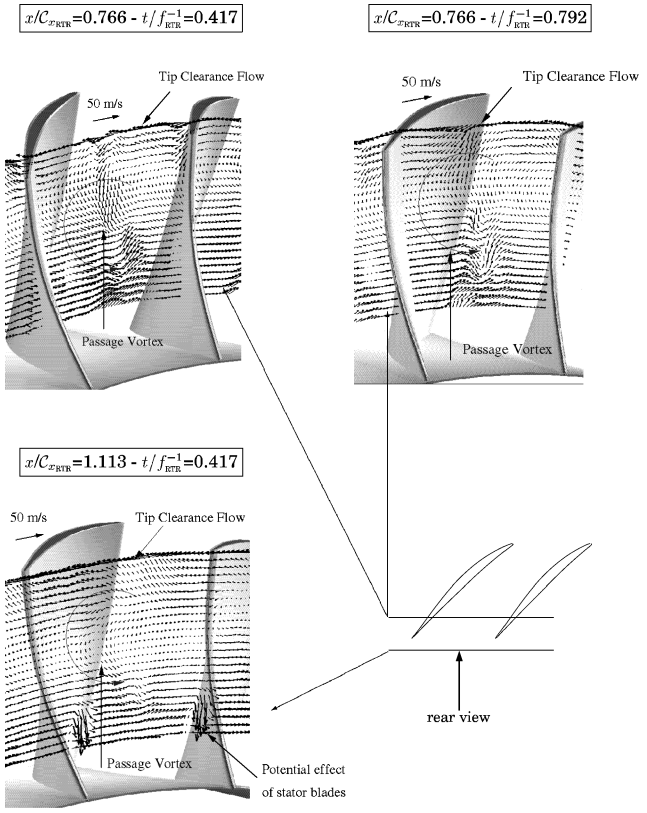

Fig. 9 Vector fields of the radial and tangential spatiotemporal fluctuations of the relative phase-averaged velocity at the outlet of the rotor; $\dot{m} = 9.0$ kg · s^{-1}.

and radial components of the velocity v_R, v_θ are presented at two different axial locations (Fig. 9). At $x/\mathcal{C}_{x_{RTR}} = 0.766$, the disturbances caused by the clearance flow between the rotor-blade tips and the casing become discernible. A passage vortex, rotating contrary to the rotor direction, is observed in the upper part of the channel. At $x/\mathcal{C}_{x_{RTR}} = 0.766$ and approximately midpitch, strong secondary flow phenomena in the lower part of the channel induce a fluid motion towards the upper region. These phenomena tend to vanish downstream of the moving row at $x/\mathcal{C}_{x_{RTR}} = 1.113$. At this axial location, the magnitude of the perturbations as a result of the potential effect of the stator blade is high near the hub.

Velocity Fields in the Stator

The periodic phase-averaged velocity field within the stator (Fig. 6) shows that the flow is strongly accelerated on the suction side of the blades at the row inlet (6C in Fig. 6). With the increase of the radius, the size of the region of high velocity (over 130 m · s^{-1}) decreases significantly, and the maximum value of the velocity decreases. The velocity of the main flow increases in the lower part of the channel ($h/H \leq 0.52$), where the direction of the flow is strongly influenced by the separated flow on the suction side of the blades.

The pitchwise distributions of the phase-averaged absolute velocity $\tilde{V}$ are plotted just upstream of the stator (PLANE_02) and within the fixed row (PLANE_ 06 and PLANE_30) at four radii and for two instants, (Fig. 7). Between the rows (PLANE_02-$x/\mathcal{C}_{x_{STR}} = -0.096$), the potential effects of the stator blades are clearly seen. Locally ($\theta \simeq 4. \rightarrow 2.5$ deg and $\theta \simeq 5. \rightarrow 6.5$ deg; $\rightarrow$: from $h/H = 0.32$ to $h/H = 0.90$), they induce a very strong decay ($\simeq 80$ m · s^{-1}) of the absolute velocity. In the spanwise direction, the azimuthal width of this perturbation and the mean value of the main flow velocity decrease slowly. Concerning the main flow, a gradient of velocity exists in the pitchwise direction, and this velocity difference increases from hub to casing especially because of a low deceleration of the flow in the vicinity of the blade pressure side. Inside the stator (PLANE_06-$x/\mathcal{C}_{x_{STR}} = 0.054$), the velocity gradient between both channel sides is very accentuated in the main flow, and its value reaches approximately 55 m · s^{-1}. The fluid is indeed strongly decelerated on the pressure side and even slightly accelerated on the suction side. The high incidence of the flow near the casing generates a small separation bubble at $h/H = 0.90$. At the stator exit (PLANE_30-$x/\mathcal{C}_{x_{STR}} = 0.975$), the deceleration of the flow is complete. In the main flow, the mean value of $\tilde{V}$ is approximately constant in the pitchwise direction (except at $h/H = 0.90$) and decreases in the spanwise direction from 95–98 m · s^{-1} at $h/H = 0.32$ to 82 m · s^{-1} at $h/H = 0.90$. A large separated flow region occurs on the blade suction side below $h/H = 0.52$ where negative (relative to the axial direction) values of the velocity are observed. The time variation of the velocity profiles is caused by the rotor-blade wakes. They induce a local decrease (10–15 m · s^{-1}) of the main flow velocity value downstream of the moving row (for example, PLANE_02; $t/f_{RTR}^{-1} = 0.5$) and at the stator inlet when the wakes are sliced by the blades and convected through the stator (for example, PLANE_06; $t/f_{RTR}^{-1} = 0.5$). However, the intensity of these perturbations vanishes gradually through the fixed row, and their influence is almost no longer discernible at the row outlet PLANE_30.

The periodic phase-averaged velocity and particularly the associated field show (Fig. 10) the structure of the vortices within the separated flow on the blade suction surface. The velocity value is the highest (over 60 m · s^{-1}) near the leading edge in a radially elongated region (10C in Fig. 10), which covers approximately all of the blade height. However, near the casing the velocity value is noticeably lower. A very confined spot of low velocity ($\tilde{V} \simeq 10$ m · s^{-1}) (10B in Fig. 10) is discernible in the vicinity of the casing downstream of the blade leading edge. It is easy to understand the process that induces this local velocity decrease by looking at the spanwise distribution of the velocity vectors at the stator inlet. The incidence of the flow is higher near the casing.

The high incidence of the flow generates a small separation bubble (10B in Fig. 10). Downstream of this perturbation, the reattachment of the flow occurs along the blade tip where the value of the velocity remains approximately constant.

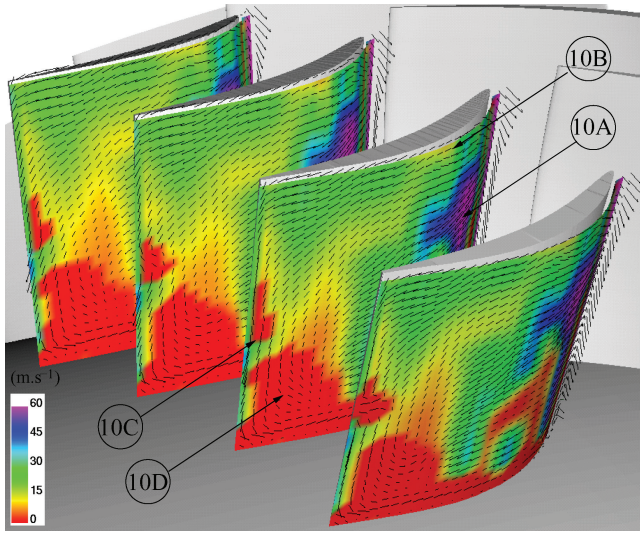

Fig. 10 Phase-averaged absolute velocity $\tilde{V}$ near the suction surface of the stator blade showing the vorticies structure in the separated flow; $\dot{m} = 9.0\ \mathrm{kg \cdot s^{-1}}$; $t/f_{\mathrm{RTR}}^{-1} = 0.0416$.

Below the midspan, the velocity value is very low in a huge region (10D in Fig. 10) close to the hub and the trailing edge. Negative values of $\tilde{V}$ characterize this region of separated flow where a strong vortex occurs. This flow structure deviates the fluid outward (see Fig. 6), and the vector field shows that the flow coming from the upper part of the channel is deviated downward. It explains why there is no separated flow on the suction side of the blade near the casing where the velocity value is approximately $20\ \mathrm{m \cdot s^{-1}}$.

An interesting flow feature is located at the trailing edge, approximately at midspan, where a small spot (10C in Fig. 10) of very low velocity is observed. The flow direction in this spot depends on the size of the vortex structure (10D in Fig. 10). When the vortex (10D in Fig. 10) is large, the flow in this spot (10C in Fig. 10) is deviated downwards. In the other cases, which means in one channel over two, the flow (10C in Fig. 10) goes around the trailing edge from the pressure side to the suction side without being deviated in the radial direction. A quite similar phenomenon can be identified at the trailing edge near the hub.

Additional information about the structure of the vortices within the stator channels is provided by the vector field of the tangential and radial components of the velocity (Fig. 11). They are plotted at two axial sections corresponding to 69.4 and 91.8% of the axial chord $C_{x_{\mathrm{STR}}}$ of the stator blades. At the first location, a vortex is visible on the blade suction side (S.S) near the casing. It induces a strong radial flow along the blade wall from tip to hub. Outside the boundary layer of the blade suction side, in the lower part of the channel, the flow is deviated in the pitchwise direction towards the pressure side (P.S). In the vicinity of the pressure side, the radial deviation of the flow increases, and a second vortex structure is formed in the upper channel part near the pressure side.

The consequences of such a flow organization are observed near the exit of the row ($x/C_{x_{\mathrm{STR}}} = 0.918$). The suction-side casing corner vortex is substantially wider, and its core has slightly moved downwards and away from the blade wall. The smaller second vortex, which rotates clockwise, is now well developed on the pressure side. This vortex is probably responsible for the low-velocity spot (10C in Fig. 10) at midspan on the trailing edge near the suction side. In the suction-side hub corner, a third vortex is generated by the combination of the flow going round the trailing edge at midradius and of the fluid motion induced by the vortex located above.

Reynolds-Stress Components

To quantify the intensity and the structure of the turbulence within the CME_2 compressor, the pitchwise distributions of the nondimensional phase-averaged Reynolds-stress components $\tilde{\tau}_{xx}$, $\tilde{\tau}_{\theta\theta}$, and $\tilde{\tau}_{x\theta}$ are plotted at two radial positions $h/H = 0.52$ and 0.90 and for two instants of the blade passing period $t = 0\%$ of f_{RTR}^{-1} and 50% of f_{RTR}^{-1}

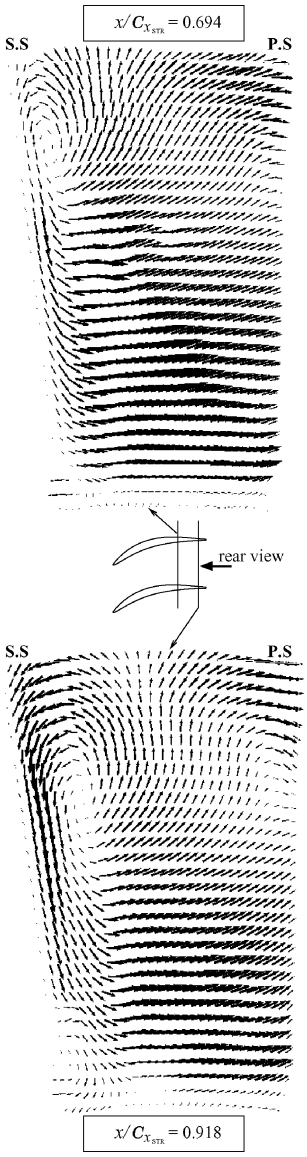

Fig. 11 Rear views of the blade-to-blade vector fields of the tangential and radial components of the absolute phase-averaged velocity in the stator row; $\dot{m} = 9.0\ \mathrm{kg \cdot s^{-1}}$, $t/f_{\mathrm{RTR}}^{-1} = 0.0416$; (P.S, pressure side; S.S, suction side).

(Fig. 12). The components, including the radial fluctuation, were also evaluated. But, as indicated earlier, very high values of $\tilde{\tau}_{xR}$, $\tilde{\tau}_{R\theta}$, $\tilde{\tau}_{\mathrm{RR}}$ were obtained. Indeed, previous studies showed[13] that the turbulence intensity is higher in the radial direction in the secondary flows, the leakage flow, and in the wake regions. The present results seem to confirm this observation, but the values are excessively high, and their accuracy is questionable. Because of the position of the volumes of measurement relative to the compressor frame, the measurement of the velocity fluctuation in the radial direction is the most difficult to perform. Fortunately, the other components of the Reynolds tensor are sufficiently accurately estimated. The level of the stress components is the highest at $h/H = 0.90$ because this region is found to be dominated by flow disturbances. Often, the tangential component $\tilde{\tau}_{\theta\theta}$ reaches higher levels than the other considered components. This is particularly true at the inlet of the rows (rotor: PLANE_51; stator: PLANE_06), where the change of the flow direction is the more obvious. Thus, at the rotor inlet (PLANE_51) and $h/H = 0.52$, the intensities of $\tilde{\tau}_{xx}$ and $\tilde{\tau}_{x\theta}$ are very low, whereas the value of $\tilde{\tau}_{\theta\theta}/U^2$ often exceeds 0.002 because the fluid is suddenly strongly deviated in the azimuthal direction by the moving blades. Near the row exit (PLANE_66), at midspan, the value of $\tilde{\tau}_{\theta\theta}$ is very low as the flow is less destabilized in the pitchwise direction at this axial location. At $h/H = 0.90$, from PLANE_51 to PLANE_66, the azimuthal evolution of the three stress components exhibits large fluctuations because of the complex structure of the flow in the vicinity of the casing (viscous effects, leakage flow, flow

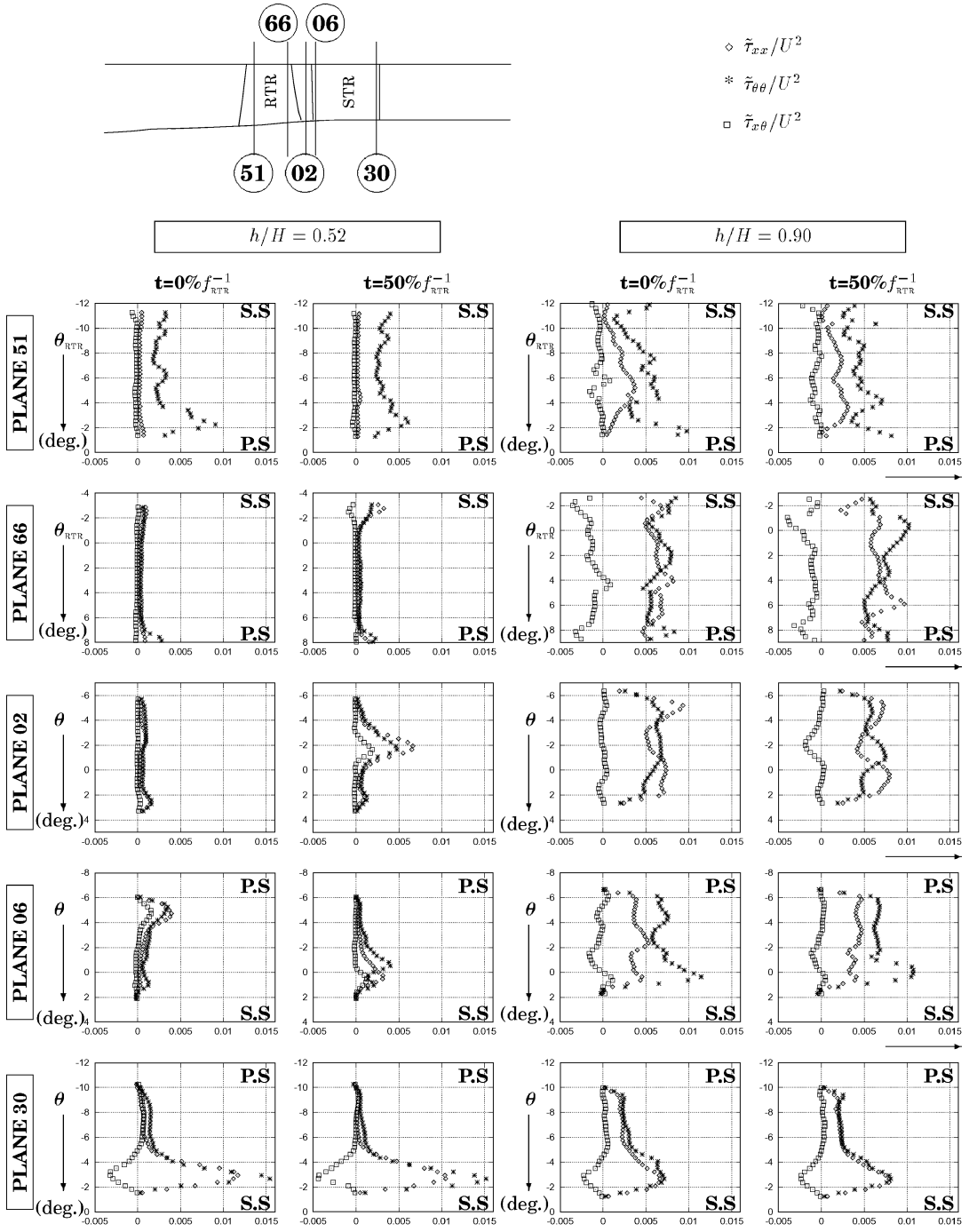

Fig. 12 Phase-averaged Reynolds-stress components $\tilde{\tau}_{xx}$, $\tilde{\tau}_{\theta\theta}$; $\tilde{\tau}_{x\theta}$; $\dot{m} = 9.0\ \mathrm{kg \cdot s^{-1}}$ (from left to right: 1st column, $h/H = 0.52$, $t = 0\%\, f_{\mathrm{RTR}}^{-1}$; 2nd column, $h/H = 0.52$, $t = 50\%\, f_{\mathrm{RTR}}^{-1}$; 3rd column, $h/H = 0.90$, $t = 0\%\, f_{\mathrm{RTR}}^{-1}$; 4th column; $h/H = 0.90$, $t = 50\%\, f_{\mathrm{RTR}}^{-1}$).

disturbances). At PLANE_02, between the two rows, the wake of the rotor blade induces a local increase of the three stress components at midspan when $t = 50\% f_{\mathrm{RTR}}^{-1}$. Within the wake, the turbulence level tends to be higher in the azimuthal direction. This is also observed in the region close to the casing where a peak of $\tilde{\tau}_{\theta\theta}$ is caused by the trace of a distorted rotor wake. Inside the stator, near the inlet (PLANE_06) at midspan, local increases of the value of the three components express the passage of a sliced rotor-blade wake. Near the blade walls (S.S and P.S), the level of the stress components remains very low. At $h/H = 0.90$, the separation of the flow on the suction side induces a spectacular increase of $\tilde{\tau}_{\theta\theta}$ and $\tilde{\tau}_{xx}$.

For the same reason, the region of the separated flow can be identified near the stator outlet, PLANE_30. As already mentioned, the amplitude of this phenomenon is considerably lower near the casing; it is confirmed by the decay of the peaks at $h/H = 0.90$. Outside of the separation region, the turbulence level in the main flow is remarkably low at midspan while the flow disturbance level remains higher at $h/H = 0.90$, but without discernible fluctuation. Thus, everywhere downstream of the moving row, the values of $\tilde{\tau}_{xx}$ and $\tilde{\tau}_{\theta\theta}$ are higher near the casing. However, outside of the separation on the suction side of the stator blade, the mean value of $\tilde{\tau}_{xx}$ decreases continuously downstream of the rotor while the mean value of $\tilde{\tau}_{\theta\theta}$ increases between PLANE_02 and PLANE_06 at $h/H = 0.90$. The overdeviation of the flow near the casing explains this increase of the turbulence level in the azimuthal direction at the stator inlet. Then, the turning and the homogenization of the main flow through the stator induce a decrease of the mean values of $\tilde{\tau}_{xx}$ and $\tilde{\tau}_{\theta\theta}$, which is more effective at $h/H = 0.90$.

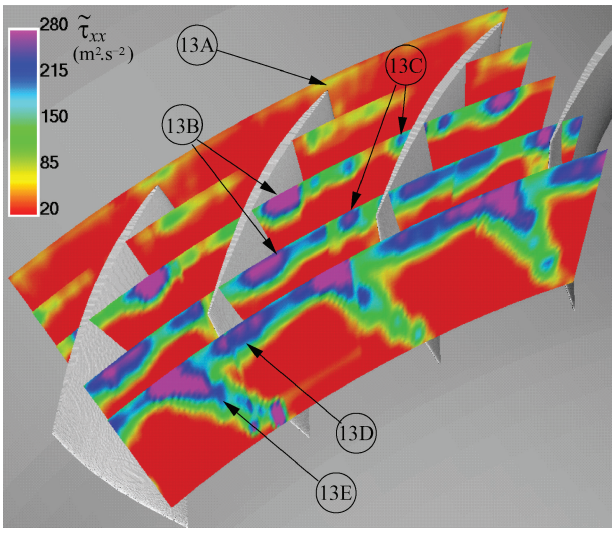

Fig. 13 Phase-averaged Reynolds-stress component $\tilde{\tau}_{xx}$ within the stator row; $x/C_{x_{RTR}} = -0.014$, 0.246, 0.506, 0.809, and 1.069, $\dot{m} = 9.0\ \text{kg} \cdot \text{s}^{-1}$, $t/f_{RTR}^{-1} = 0.375$.

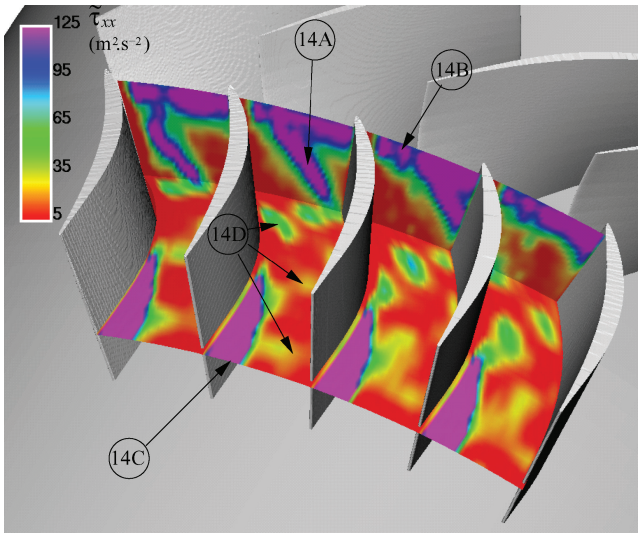

Fig. 14 Phase-averaged Reynolds-stress component $\tilde{\tau}_{xx}$ within the stator row; $x/C_{x_{STR}} = 0.054$ and $h/H = 0.36$, $\dot{m} = 9.0\ \text{kg} \cdot \text{s}^{-1}$, $t/f_{RTR}^{-1} = 0.375$.

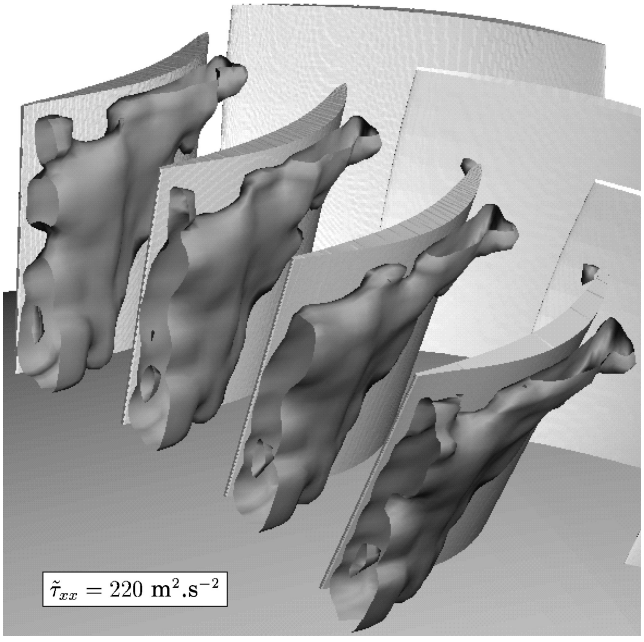

Fig. 15 Isosurface at level $= 220\ \text{m}^2 \cdot \text{s}^{-2}$ of the phase-averaged Reynolds-stress component $\tilde{\tau}_{xx}$ near the suction surface of the stator blades showing the three-dimensional structure of the separated flow; $\dot{m} = 9.0\ \text{kg} \cdot \text{s}^{-1}$, $t/f_{RTR}^{-1} = 0.375$.

The isocontours of the axial component of the Reynolds stress $\tilde{\tau}_{xx}$ are presented (Fig. 13) at five axial locations distributed from just upstream of to downstream of the rotor when $t = 37.5\%$ of f_{RTR}^{-1}. Three planes show the values inside the rotor channels. A local perturbation caused by the potential effect of the moving blades is discernible just upstream of the row (13A in Fig. 13), and the high level of the flow disturbance within the blade wakes is observed (13E in Fig. 13) downstream of the rotor. But, it is more interesting to analyze the disturbance of the flow near the casing. A spot of high level of turbulence (relative to the axial direction) appears in the vicinity of the leading edge near the blade pressure side. It extends gradually inwards and covers all of the channel width at approximately the midchord. In fact, at least two kinds of phenomena seem to occur in this region: 1) scraping structures (13B in Fig. 13) often with several cores that include a spot of very high intensity ($\tilde{\tau}_{xx} \geq 300\ \text{m}^2 \cdot \text{s}^{-2}$) and develop at the pressure-side casing corner, and 2) confined spots (13C in Fig. 13) of lower intensity induced by the secondary flow through the tip clearance of the rotor blades. Because of the low mass-flow rate, to the small relative clearance size and essentially to the low pressure ratio, the influence of the leakage flow remains limited, and it moves away from the blades by expanding gently.

The value of $\tilde{\tau}_{xx}$ within the scraping structure (13B in Fig. 13) decreases in the streamwise direction during the azimuthal expansion of this structure, which seems to disintegrate progressively into smaller ones, as suggested by the observation of several spots (13D in Fig. 13) downstream of the row. The azimuthal location of the core of the scraping structure in the upstream part of the channel varies from one channel to another. Sometimes it is created very close to the blade pressure side, and, in the adjacent channel, it develops more inwards. Because of the low mass-flow rate, the main flow occupies the lower part of the channels. Such a main flow behavior induces the development of flow perturbations near the casing caused by the viscous effects and by the tip clearance flow. This observation could be compared with those reported by previous studies.[27,28] Without achieving rotating stall conditions, the margin to the stall is small here. It probably explains why the upper part of the rotor channels is found to be dominated by strong flow disturbances.

The complex nature of the well-established separated flow in the stator can also be assessed by looking at the phase-averaged Reynolds-stress axial component $\tilde{\tau}_{xx}$ (Fig. 14). Spatial distributions of $\tilde{\tau}_{xx}$ are presented just downstream of the stator inlet ($x/C_{x_{STR}} = 0.054$) and within the stator at $h/H = 0.36$. At the row inlet, the highest turbulence level is obviously achieved in the oblique wakes of the rotor blades (14A in Fig. 14) and in the mixing region near the casing (14B in Fig. 14). The blade-to-blade field of the axial Reynolds-stress component at constant radius shows that the highest turbulence level is observed in the separated flow region (14C in Fig. 14) on the suction sides of the blades. The thickness of the disturbance associated with this phenomenon is estimated to nearly one-third of the channel width at $h/H = 0.36$. The other regions of high turbulence level (14D in Fig. 14) ($\tilde{\tau}_{xx} \geq 20\ \text{m}^2 \cdot \text{s}^{-2}$) indicate the location of the sliced rotor wakes convected through the stator. The traces of the wakes are fragmented and are characterized by a succession of spots of higher intensity obliquely distributed in the pitchwise direction. Their intensity decreases very quickly in the streamwise direction. This explains why the interaction between the convected wakes and the separated flow is not clearly discernible. The passage of a wake only causes a periodic slight variation of the thickness of the separated region.

The large three-dimensional structure of the separated flow on the stator-blade suction side appears clearly by looking at the isosurface $\tilde{\tau}_{xx} = 220\ \text{m}^2 \cdot \text{s}^{-2}$ (Fig. 15). The flow is not very disturbed in the region very close to the casing. But immediately below, the

turbulence relative to the axial direction increases from the leading edge up to the row exit and downward to the hub. At the outlet, the perturbation occupies most of the channel height and extends fairly far inside the channel. Because of a mechanism already described (Figs. 10 and 11), the fluid radially deviated downwards along the blade generates this complex, strong, and thick vortex structure, which is well illustrated here.

Conclusions

The flow in an axial subsonic single-stage compressor was investigated using a three-dimensional laser Doppler velocimeter at an off-design mass-flow rate close to the compressor rotating stall limit. The measurements of the velocity and velocity fluctuations were performed within the entire stage at the nodes of a refined grid including more than 8000 points of measurements. A detailed database of the unsteady phase-averaged flowfield was obtained to provide experimental data for accurate validation of computational-fluid-dynamics results. The features of the three-dimensional flowfield inside the stage are examined in terms of phase-averaged velocity and Reynolds-stress distributions. The particular behavior of the flow within the different parts of the compressor is observed and analyzed for such off-design critical conditions of operation. In the rotor row, the reduction of the mass-flow rate essentially affects the region close to the casing where a complex flow disturbance is observed. It is mainly created by scraping structures generated at the blade pressure-side casing corner at the rotor inlet, but the combination of these structures with the tip leakage flow is also underlined. Consequently, the main flow occurs in the lower part of the rotor channels. However, it seems difficult to accurately define the influence of these disturbed structures on the flow downstream of the rotor.

The flow in the stator row is governed by high incidence effects especially near to the casing. A massive and well-established separated flow, generated at the leading-edge casing corner, is observed on the blade suction side. The analysis of the wide three-dimensional vortical structure, induced by this separation, shows that the fluid is strongly deviated from the casing to the hub along the stator-blade suction side. This fluid motion creates vortices on both channel sides in the upper part of the stator. Periodically, at midspan, a small quantity of fluid is aspirated from the pressure side to the suction side at the blade trailing edge because of the strong influence of the separated flow. Otherwise, it is observed that the interaction between the convected rotor wakes and the separated flow-induced confined perturbations expressed as small and periodic increases of the separation width. Such three-dimensional and quite steady phenomena explain why the flow is often remarkably stable despite its vicinity of the rotating stall limit.

Acknowledgments

The authors are greatful to the Consortium Industrie Recherche en Turbomachines and the supporting companies: Société Nationale d'Étude et de Construction de Moteurs d'Aviation, Électricité De France. The support of the Centre National de la Recherche Scientifique and of the Région Île de France is also acknowleged. The technical assistance of J.-P. Dalac has been greatly appreciated. The authors are listed alphabetically.

References

[1]Gerolymos, G. A., Michon, G.-J., and Miton, H., "Experimental and Computational Investigation of the Unsteady Aerodynamics of an Axial Compressor Stage," *Proceedings of the 5th European Conference on Turbomachinery, Fluid Dynamics and Thermodynamics*, edited by M. Stastny, C. H. Sieverding, and G. Bois, Local Conference Organising Committee, Prague, 2003, pp. 257–266.

[2]Wisler, D. C., and Mossey, P. W., "Gas Velocity Measurements Within a Compressor Rotor Passage Using the Laser Doppler Velocimeter," American Society of Mechanical Engineers, 72-WA/GT-2, 1972.

[3]Chesnakas, C. J., and Dancey, C. L., "Three Component Measurements in an Axial Flow Compressor," *Journal of Propulsion and Power*, Vol. 6, No. 4, 1990, pp. 471–481.

[4]Stauter, R. C., "Measurements of the Three-dimensional Tip Region Flowfield in an Axial Compressor," *Journal of Turbomachinery*, Vol. 115, No. 3, 1993, pp. 468–476.

[5]Hathaway, M. D., Chriss, R. M., Wood, J. R., and Strazisar, A. J., "Experimental and Computational Investigation of the NASA Low-Speed Centrifugal Compressor Flow Field," *Journal of Turbomachinery*, Vol. 115, No. 3, 1993, pp. 527–542.

[6]Faure, T. M., Michon G.-J., Miton, H., and Vassilieff, N., "Laser Doppler Anemometry Measurements in an Axial Compressor Stage," *Journal of Propulsion and Power*, Vol. 17, No. 3, 2001, pp. 481–491.

[7]Ubaldi, M., Zunino, P., and Cattanei, A., "Relative Flow and Turbulence Measurements Downstream of a Backward Centrifugal Impeller," *Journal of Turbomachinery*, Vol. 115, No. 3, 1993, pp. 543–551.

[8]Pinarbasi, A., and Johnson, M. W., "Detailed Stress Tensor Measurements in a Centrifugal Compressor Vaneless Diffuser," *Journal of Turbomachinery*, Vol. 118, No. 2, 1996, pp. 394–399.

[9]Ravindranath, A., and Lakshminarayana, B., "Structure and Decay Characteristics of Turbulence in the Near and Far-Wake of a Moderately Loaded Compressor Rotor-Blade," *ASME Journal of Engineering for Power*, Vol. 103, 1981, pp. 131–140.

[10]Inoue, M., and Kuroumaru, M., "Three-Dimensional Structure and Decay of Vortices Behind an Axial Flow Rotating Blade Row," *Journal of Engineering for Gas Turbines and Power*, Vol. 106, 1984, pp. 561–569.

[11]Sentker, A., Riess, W., "Experimental Investigation of Turbulent Wake-Blade Interaction in Axial Compressor," *International Journal of Heat and Fluid Flow*, Vol. 21, No. 3, 2000, pp. 285–290.

[12]Zaccaria, M. A., and Lakshminarayana, B., "Unsteady Flow Field due to Nozzle Wake Interaction with the Rotor in an Axial Flow Turbine: Part 1: Rotor Exit Flow Field, Part 2: Rotor Exit Flow Field," *Journal of Turbomachinery*, Vol. 119, No. 2, 1997, pp. 201–224.

[13]Ristic, D., Lakshminarayana, B., and Chu, S., "Three-Dimensional Flowfield Downstream of an Axial Flow Turbine Rotor," *Journal of Propulsion and Power*, Vol. 15, No. 2, 1999, pp. 334–344.

[14]Foley, A. C., and Ivey, P. C., "Measurement of Tip Clearance Flow in a Multistage Axial Flow Compressor," *Journal of Turbomachinery*, Vol. 118, No. 4, 1996, pp. 211–217.

[15]Suder, K. L., Chima, R. V., Strazisar, A. J., and Roberts, W. B., "The Effects of Adding Roughness and Thickness to a Transonic Axial Compressor Rotor," *Journal of Turbomachinery*, Vol. 117, No. 4, 1995, pp. 491–505.

[16]Suder, K. L., and Celestina, M. L., "Experimental and Computational Investigation of the Tip Clearance Flow in a Transonic Compressor Rotor," *Journal of Turbomachinery*, Vol. 118, No. 2, 1996, pp. 218–229.

[17]Edmonds, J. D., and Wiseall, M. L., "Recent Developments in the Application of Laser Doppler Anemometry to Compressor Rigs," 90th Symposium on Advanced Non-intrusive Instrumentation for Propulsion Engines, AGARD, 1997.

[18]Hah, C., and Loellbach, J., "Development of Hub Corner Stall and Its Influence on the Performance of an Axial Compressor Blades Rows," *Journal of Turbomachinery*, Vol. 121, No. 1, 1999, pp. 67–77.

[19]Schulz, H. D., and Gallus, H. E., "Experimental Investigation of the Three-Dimensional Flows in an Annular Compressor Cascade," *Journal of Turbomachinery*, Vol. 110, No. 4, 1988, pp. 467–478.

[20]Popovski, P., and Lakshminarayana, B., "Laser Anemometer Measurements in a Compressor Rotor Flowfield at Off-design Conditions," *AIAA Journal*, Vol. 24, No. 8, 1986, pp. 1337–1345.

[21]Schreeve, R. P., Elazar, Y., Dreon, J. W., and Baydar, A., "Wake Measurements and Loss Evaluation in a Controlled Diffusion Compressor Cascade," *Journal of Turbomachinery*, Vol. 113, No. 4, 1991, pp. 591–599.

[22]Pradère, T., "Contribution au Développement de la Vélocimétrie Laser Doppler dans les Turbomachines," Ph.D. Dissertation, Univ. Pierre et Marie Curie, Paris, Dec. 1998.

[23]Vassilieff, N., "Analyse par Vélocimétrie Laser Tridimensionnelle de l'Écoulement dans un Compresseur Axial," Ph.D. Dissertation, Univ. Pierre et Marie Curie, Paris, Nov. 2000.

[24]Adamczyk, J. J., "Aerodynamic Analysis of Multistage Turbomachinery Flows in Support of Aerodynamic Design," *Journal of Turbomachinery*, Vol. 122, No 2, 2000, pp. 189–224.

[25]Faure, T. M., Miton, H., and Vassilieff, N., "A Laser Doppler Anemometry Technique for Reynolds Stresses Measurement" *Experiments in Fluids*, Vol. 37, No. 3, 2004, pp. 465–467.

[26]Gerolymos, G. A., Michon, G.-J., and Neubauer, J., "Analysis and Application of Chorochronic Periodicity in Turbomachinery Rotor/Stator Interaction Computations," *Journal of Propulsion and Power*, Vol. 18, No. 6, 2001, pp. 1139–1152.

[27]Inoue, M., Kuroumaru, M., and Ando, Y., "Pressure Fluctuation on the Casing Wall of Isolated Axial Compressor Rotors at Low Flow Rate," *Journal of Turbomachinery*, Vol. 115, No. 1, 1993, pp. 19–27.

[28]Mailach, R., Lehmann, I., and Vogeler, K., "Rotating Instabilities in an Axial Compressor Originating from the Fluctuating Blade Tip Vortex," *Journal of Turbomachinery*, Vol. 123, No. 3, 2001, pp. 453–463.